PHYSICAL REVIEW B **95**, 125136 (2017)

Multiple Weyl points and the sign change of their topological charges in woodpile photonic crystals

Ming-Li Chang, Meng Xiao, Wen-Jie Chen, and C. T. Chan*

Department of Physics, Institute for Advanced Study, The Hong Kong University of Science and Technology, Hong Kong, China

(Received 1 August 2016; revised manuscript received 20 February 2017; published 29 March 2017)

We show that Weyl points with topological charges 1 and 2 can be found in very simple chiral woodpile photonic crystals and the distribution of the charges can be changed by changing the material parameters without altering space-group symmetry. The underlying physics can be understood through a tight-binding model. Gapless surface states and their backscattering immune properties also are demonstrated in these systems. Obtaining Weyl points in these easily fabricated woodpile photonic crystals will facilitate the realization of Weyl point physics in optical and IR frequencies.

DOI: 10.1103/PhysRevB.95.125136

I. INTRODUCTION

Recently, topological systems carrying Weyl points have attracted a lot of attention [1–15]. A Weyl point can be viewed as a magnetic monopole in momentum space that carries a topological charge and acts as a quantized source or sink of Berry flux [16]. Weyl points are virtually indestructible, unless two Weyl nodes of opposite charges are tuned to annihilate each other. Systems with broken parity or time-reversal symmetries can potentially carry Weyl points, but details about the structure and material are important.

It is perhaps the lack of a simple rule to generate Weyl points that has made classical wave systems designed to exhibit Weyl nodes so structurally complex [9,11] and it is unlikely that these structures can be made at high frequencies. The natural question to ask is as follows: Can we find simple periodic nanostructures that carry Weyl points? For high-frequency applications, the most popular photonic crystal (PC) structures are the "woodpile" structures [17], composed of stacked layers of rods. Most of the three-dimensional (3D) PCs that have been fabricated to date are indeed woodpile structures [18–22]. We will show that very simple chiral woodpile PCs carry Weyl points. Such woodpile structures have been fabricated [23]. We find that these structures not only support Weyl points with topological charge 1, but also carry Weyl points with topological charge 2. We confirm the existence of Weyl points in woodpile PCs using the tight-binding model (TBM) [24], the $\vec{k}\cdot\vec{p}$ method [25], and numerical computation. In addition, the distribution of topological charges can be controlled by varying the permittivity distribution while keeping the same symmetry. Such a topological sign change can lead to the presence or absence of gapless surface states on specific surface terminations.

II. TIGHT-BINDING MODEL OF WOODPILE PHOTONIC CRYSTALS

The chiral woodpile PC has a unit cell as shown in Fig. 1(a), consisting of three layers of rods (cyan) with width b and height h, and each layer is rotated 120° clockwise from the layer below, twisting up in the z direction while forming a triangular lattice on the x-y plane. The length and height of a unit cell are d and p, where $p = 3h$. We first consider the air-in-metal configuration corresponding to air rods drilled into a perfect electric conductor (PEC) background. The computed eigenfield patterns show that the low-frequency modes are confined to the crossing points on the rotation axis so that the band dispersion can be described satisfactorily by the TBM. The simplest TBM that captures the network connectivity is illustrated in Fig. 1(b), showing three "atoms" stacked along the central rotation axis and connected by two kinds of nearest-neighbor (NN) hopping: in-plane intralayer hopping [blue bonds in Fig. 1(b)] and direct interlayer hopping (orange bonds). We also include next-nearest-neighbor (NNN) hopping of which the red bond in Fig. 1(b) is an example. The TBM Hamiltonian of the system is

$$H = \sum_{i,k} \varepsilon a^{\dagger}_{i,k} a_{i,k} + \sum_{\langle i,j\rangle} t_{n1} a^{\dagger}_{i,k} a_{j,k} + \text{H.c.} + \sum_{i,k} t_{n2} a^{\dagger}_{i,k} a_{j,k+1} + \text{H.c.} + \sum_{\langle\langle i,j\rangle\rangle} t_{nnn} a^{\dagger}_{i,k} a_{j,k+1} + \text{H.c.}, \quad (1)$$

where a ($a^{\dagger}$) is the annihilation (creation) operator and the first and second subscripts represent the position in each layer and the layer number, respectively. $\langle i,j\rangle$ represents an intralayer NN lattice, and $\langle\langle i,j\rangle\rangle$ denotes an NNN lattice as shown in Fig. 1(b). The first term represents the on-site energy. The second summation gives the NN intralayer hopping with hopping strength t_{n1}. The third summation describes the NN interlayer hopping with hopping strength t_{n2}. The last summation represents the NNN hopping.

To write down the matrix form of the tight-binding Hamiltonian in the momentum space, we consider the three-atom model as shown in Fig. 1(b). Each atom in the first layer connects with the NN atoms in the same layer with blue rods with hopping strength t_{n1}. Therefore the overlap matrix element is

$$H_{11} = t_{n1}[\exp(ik_y d) + \exp(-ik_y d)] = 2t_{n1}\cos(k_y d). \quad (2)$$

Similarly, the intralayer hopping between the atoms in the second and third layers can be written as

$$\begin{aligned} H_{22} &= t_{n1}\{\exp[i(\sqrt{3}k_x - k_y)d/2] \\ &\quad + \exp[-i(\sqrt{3}k_x - k_y)d/2]\} \\ &= 2t_{n1}\cos[(\sqrt{3}k_x - k_y)d/2], \end{aligned} \quad (3)$$

*phchan@ust.hk

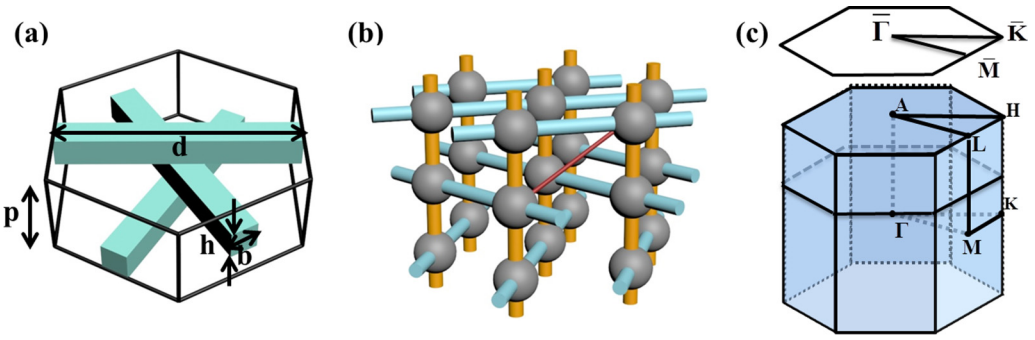

FIG. 1. (a) The unit cell contains three layers of rods. (b) The tight-binding model with atoms connected by "bonds." (c) The reciprocal space of (a).

$$H_{33} = t_{n1}\{\exp[i(\sqrt{3}k_x + k_y)d/2] + \exp[-i(\sqrt{3}k_x + k_y)d/2]\} = 2t_{n1}\cos[(\sqrt{3}k_x + k_y)d/2]. \quad (4)$$

The hopping between different layers includes the direct NN hopping between the atoms in adjacent layers (yellow bonds) and the NNN hoppings (red bonds). For example, the hopping between the first and the second layers can be written as

$$H_{12} = e^{-ik_z h}(t_{n2} + 2t_{nnn}\{\cos[(\sqrt{3}k_x - k_y)d/2] + \cos[(\sqrt{3}k_x + k_y)d/2]\}). \quad (5)$$

Therefore the TBM Hamiltonian in momentum space is in the form of

$$H(\mathbf{k}) = \begin{pmatrix} t_{n1}\alpha & e^{-ik_z h}[t_{n2} + t_{nnn}(\alpha+\beta)] & e^{ik_z h}[t_{n2} + t_{nnn}(\alpha+\gamma)] \\ e^{ik_z h}[t_{n2} + t_{nnn}(\beta+\alpha)] & t_{n1}\beta & e^{-ik_z h}[t_{n2} + t_{nnn}(\beta+\gamma)] \\ e^{-ik_z h}[t_{n2} + t_{nnn}(\gamma+\alpha)] & e^{ik_z h}[t_{n2} + t_{nnn}(\gamma+\beta)] & t_{n1}\gamma \end{pmatrix}, \quad (6)$$

where $\alpha = 2\cos(k_y d)$, $\beta = 2\cos[(\sqrt{3}k_x - k_y)d/2]$ and $\gamma = 2\cos[(\sqrt{3}k_x + k_y)d/2]$. ΓA and KH are the directions with screw symmetry, which ensures that two bands are degenerate at one frequency at K and Γ points. To investigate the topological properties of the bands, we expand the TBM Hamiltonian around $\Gamma(0,0,0)$, $A(0,0,\pi/p)$, $K(2\pi/\sqrt{3}d, 2\pi/3d, 0)$, and $H(2\pi/\sqrt{3}d, 2\pi/3d, \pi/p)$ [see Fig. 1(c)], which gives

$$H(K+\mathbf{p}) = \begin{pmatrix} t_{n1}f_{K1} & f_{z1}[t_{n2} + t_{nnn}(f_{K1} + f_{K2})] & f_{z2}[t_{n2} + t_{nnn}(f_{K1} + f_{K3})] \\ f_{z2}[t_{n2} + t_{nnn}(f_{K2} + f_{K1})] & t_{n1}f_{K2} & f_{z1}[t_{n2} + t_{nnn}(f_{K2} + f_{K3})] \\ f_{z1}[t_{n2} + t_{nnn}(f_{K3} + f_{K1})] & f_{z2}[t_{n2} + t_{nnn}(f_{K3} + f_{K2})] & t_{n1}f_{K3} \end{pmatrix}, \quad (7a)$$

$$H(\Gamma+\mathbf{p}) = \begin{pmatrix} t_{n1}f_{G1} & f_{z1}[t_{n2} + t_{nnn}(f_{G1} + f_{G2})] & f_{z2}[t_{n2} + t_{nnn}(f_{G1} + f_{G3})] \\ f_{z2}[t_{n2} + t_{nnn}(f_{G2} + f_{G1})] & t_{n1}f_{G2} & f_{z1}[t_{n2} + t_{nnn}(f_{G2} + f_{G3})] \\ f_{z1}[t_{n2} + t_{nnn}(f_{G3} + f_{G1})] & f_{z2}[t_{n2} + t_{nnn}(f_{G3} + f_{G2})] & t_{n1}f_{G3} \end{pmatrix}, \quad (7b)$$

$$H(H+\mathbf{p}) = \begin{pmatrix} t_{n1}f_{K1} & e^{-i\pi/3}f_{z1}[t_{n2} + t_{nnn}(f_{K1} + f_{K2})] & e^{i\pi/3}f_{z2}[t_{n2} + t_{nnn}(f_{K1} + f_{K3})] \\ e^{i\pi/3}f_{z2}[t_{n2} + t_{nnn}(f_{K2} + f_{K1})] & t_{n1}f_{K2} & e^{-i\pi/3}f_{z1}[t_{n2} + t_{nnn}(f_{K2} + f_{K3})] \\ e^{-i\pi/3}f_{z1}[t_{n2} + t_{nnn}(f_{K3} + f_{K1})] & e^{i\pi/3}f_{z2}[t_{n2} + t_{nnn}(f_{K3} + f_{K2})] & t_{n1}f_{K3} \end{pmatrix}, \quad (7c)$$

$$H(A+\mathbf{p}) = \begin{pmatrix} t_{n1}f_{G1} & e^{-i\pi/3}f_{z1}[t_{n2} + t_{nnn}(f_{G1} + f_{G2})] & e^{i\pi/3}f_{z2}[t_{n2} + t_{nnn}(f_{G1} + f_{G3})] \\ e^{i\pi 3}f_{z2}[t_{n2} + t_{nnn}(f_{G2} + f_{G1})] & t_{n1}f_{G2} & e^{-i\pi/3}f_{z1}[t_{n2} + t_{nnn}(f_{G2} + f_{G3})] \\ e^{-i\pi/3}f_{z1}[t_{n2} + t_{nnn}(f_{G3} + f_{G1})] & e^{i\pi/3}f_{z2}[t_{n2} + t_{nnn}(f_{G3} + f_{G2})] & t_{n1}f_{G3} \end{pmatrix}, \quad (7d)$$

where

$$f_{K1} = -1 - \sqrt{3}p_y d, \quad f_{K2} = -1 - \sqrt{3}/2(p_x - p_y)d, \quad f_{K3} = -1 + \sqrt{3}/2(p_x + p_y)d,$$
$$f_{G1} = 2\big(1 - p_y^2 d^2/2\big), \quad f_{G2} = 2\big(1 - \big(3p_x^2/4 - \sqrt{3}p_x p_y/2 + p_y^2/4\big)\big)d^2/2,$$
$$f_{G3} = 2\big[1 - \big(3p_x^2/4 + \sqrt{3}p_x p_y/2 + p_y^2/4\big)d^2/2\big], \quad f_{z1} = 1 - i\,p_z h, \quad f_{z2} = 1 + i\,p_z h, \quad (8)$$

where p_x, p_y, and p_z are momentum components near the degenerate point.

If we plot the band dispersions near these high-symmetry points, two bands become degenerate at the high-symmetry point, and another band is at a different frequency. First we take the unitary transform of the Hamiltonian as

$$H_0 = U^{\dagger} H(\mathbf{p}) U, \tag{9}$$

where U and $U^{\dagger}$ are the eigenvectors and their complex conjugate of $H(\mathbf{p}=0)$ at these high-symmetry k points. After the unitary transformation, H_0 is now diagonal at these high-symmetry points. We assume that H_{11} is the eigenenergy of the single mode and $H_{22} = H_{33} = \mu$ at these points represents the energy of the degenerate modes. Here H_{ij} represents the ij matrix element of H_0. As the nondegenerate band is located at a different frequency, its interactions (with amplitude at most proportional to $\|\mathbf{p}\|$) with the other two degenerate modes can be treated as a perturbation. As such, the 3×3 Hamiltonian can be reduced to a 2×2 Hamiltonian near the degenerate point [26] as

$$H_{\text{eff}} = \begin{pmatrix} H_{22} & H_{23} \\ H_{32} & H_{33} \end{pmatrix} - \frac{1}{H_{11}-\mu} \begin{pmatrix} H_{21}H_{12} & H_{21}H_{13} \\ H_{31}H_{12} & H_{31}H_{13} \end{pmatrix}. \tag{10}$$

Keeping only the terms at the lowest order of p_x, p_y, and p_z, the effective Hamiltonians of the degenerate points around K, H, and Γ, A can be expressed in the basis of Pauli matrices as

$$\begin{aligned}
H(K+\mathbf{p}) &= (2t_{nnn} - t_{n1} - t_{n2})\sigma_0 + (t_{n1} - 2t_{nnn})d(p_x - 3p_y)\sigma_1/4 + \sqrt{3}(t_{n1} - 2t_{nnn})h\,p_z\sigma_2 \\
&\quad - \sqrt{3}(t_{n1} - 2t_{nnn})d(p_x + p_y)\sigma_3/4, \qquad (11a)\\
H(H+\mathbf{p}) &= (2t_{nnn} - t_{n2} - t_{n1})\sigma_0 + (t_{n1} - 2t_{nnn})[(p_x - 3p_y)d - 12p_z h]\sigma_1/8 \\
&\quad + \sqrt{3}(t_{n1} - 2t_{nnn})[(p_x - 3p_y)d + 4p_z h]\sigma_2/8 - \sqrt{3}(t_{n1} - 2t_{nnn})d(p_x + p_y)\sigma_3/4, \qquad (11b)\\
H(\Gamma+\mathbf{p}) &= \left[(2t_{n1} - t_{n2} - 4t_{nnn}) - (t_{n1} - 2t_{nnn})d^2\left(p_x^2 + p_y^2\right)/2\right]\sigma_0 + (t_{n1} - 2t_{nnn})d^2\left(\sqrt{3}p_x^2 - 2p_x p_y - \sqrt{3}p_y^2\right)\sigma_1/8 \\
&\quad + \sqrt{3}(t_{n2} + 4t_{nnn})h\,p_z\sigma_2 + (t_{n1} - 2t_{nnn})d^2\left(-p_x^2 - 2\sqrt{3}p_x p_y + p_y^2\right)\sigma_3/8, \qquad (11c)\\
H(A+\mathbf{p}) &= \left[2t_{n1} - t_{n2} - 4t_{nnn} - (t_{n1} - 2t_{nnn})d^2\left(p_x^2 + p_y^2\right)/2\right]\sigma_0 + \left[(t_{n1} - 2t_{nnn})\left(\sqrt{3}p_x^2 - 2p_x p_y - \sqrt{3}p_y^2\right)d^2\right. \\
&\quad \left. - 24(t_{n1} + 4t_{nnn})h\,p_z\right]\sigma_1/16 + \sqrt{3}\left[(t_{n1} - 2t_{nnn})\left(\sqrt{3}p_x^2 - 2p_x p_y - \sqrt{3}p_y^2\right)d^2\right. \\
&\quad \left. - 8(t_{n1} + 4t_{nnn})h\,p_z\right]\sigma_2/16 + (t_{n1} - 2t_{nnn})d^2\left(-p_x^2 - 2\sqrt{3}p_x p_y + p_y^2\right)\sigma_3/8, \qquad (11d)
\end{aligned}$$

where σ_1, σ_2, and σ_3 are the Pauli matrixes and σ_0 is a 2×2 identity matrix. The reduced Hamiltonian is in the Weyl form, linear in p_x, p_y, and p_z at K but with the second-order terms of p_x and p_y at Γ. Similar results can be obtained at H and A points as shown in Eqs. (11b) and (11d). These TBM results indicate that two Weyl points with topological charges ± 1 can be found at K and H and two Weyl points with topological charges ± 2 can be found at Γ and A [27]. The charge -2 Weyl points are protected by the combination of the screw symmetry and the time-reversal symmetry, and the different topological charges at $K(H)$ and $\Gamma(A)$ are caused by the different symmetries at these points as shown in Fig. 11. If the symmetry is reduced, the charge -2 Weyl points will break up into charge -1 nodes and will move away from the high-symmetry line.

The topological charge can be obtained by calculating the Chern number around these k points with the eigenvectors of Eqs. (11a)–(11d) with the formulas [28],

$$\Omega^n(\theta,\phi) = i \sum_{n' \neq n} \frac{\langle n|\partial H_{\text{eff}}/\partial\theta|n'\rangle\langle n'|\partial H_{\text{eff}}\partial\phi|n\rangle - (\theta \leftrightarrow \phi)}{(E_n - E_{n'})^2}, \tag{12}$$

$$C_n = \frac{1}{2\pi}\int_{s^2} d\theta\, d\phi\, \Omega^n_{\theta\phi}. \tag{13}$$

The integral is performed for a spherical surface enclosing the nodal point. The calculation of the Chern number can be simplified by changing the basis from (p_x, p_y, p_z) to (p_r, p_θ, p_ϕ), and we take $p_r = 0.01\,\pi/d$. The signs of charges at the high-symmetry points are found to be

$$C(K) = \text{sgn}(t_{n2} - 2t_{nnn}), \quad C(\Gamma) = -2\,\text{sgn}(t_{n2} + 4t_{nnn}), \tag{14a}$$

and

$$C(H) = -\text{sgn}(t_{n2} - 2t_{nnn}), \quad C(A) = 2\,\text{sgn}(t_{n2} + 4t_{nnn}). \tag{14b}$$

These TBM results indicate that Weyl points with topological charges 1 and 2, respectively, can be found at the zone boundary and the zone center, and the sign of the charge can be set by adjusting t_{n2} and t_{nnn}. It is not easy to obtain the hopping parameters without knowing the eigenmodes, but the hopping parameters in a real structure can be estimated by fitting to the full wave calculated band structure [29].

III. WEYL POINTS IN AIR-IN-METAL WOODPILE PCS

To show that Weyl points can exist in the real optical system, we calculate the 3D bands of the air-in-metal PCs with $d = 60$, $b = 24$, and $h = 30\,\mu$m using COMSOL as shown in Figs. 2(a)–2(f). Figures 2(a)–2(c) show two cones degenerate

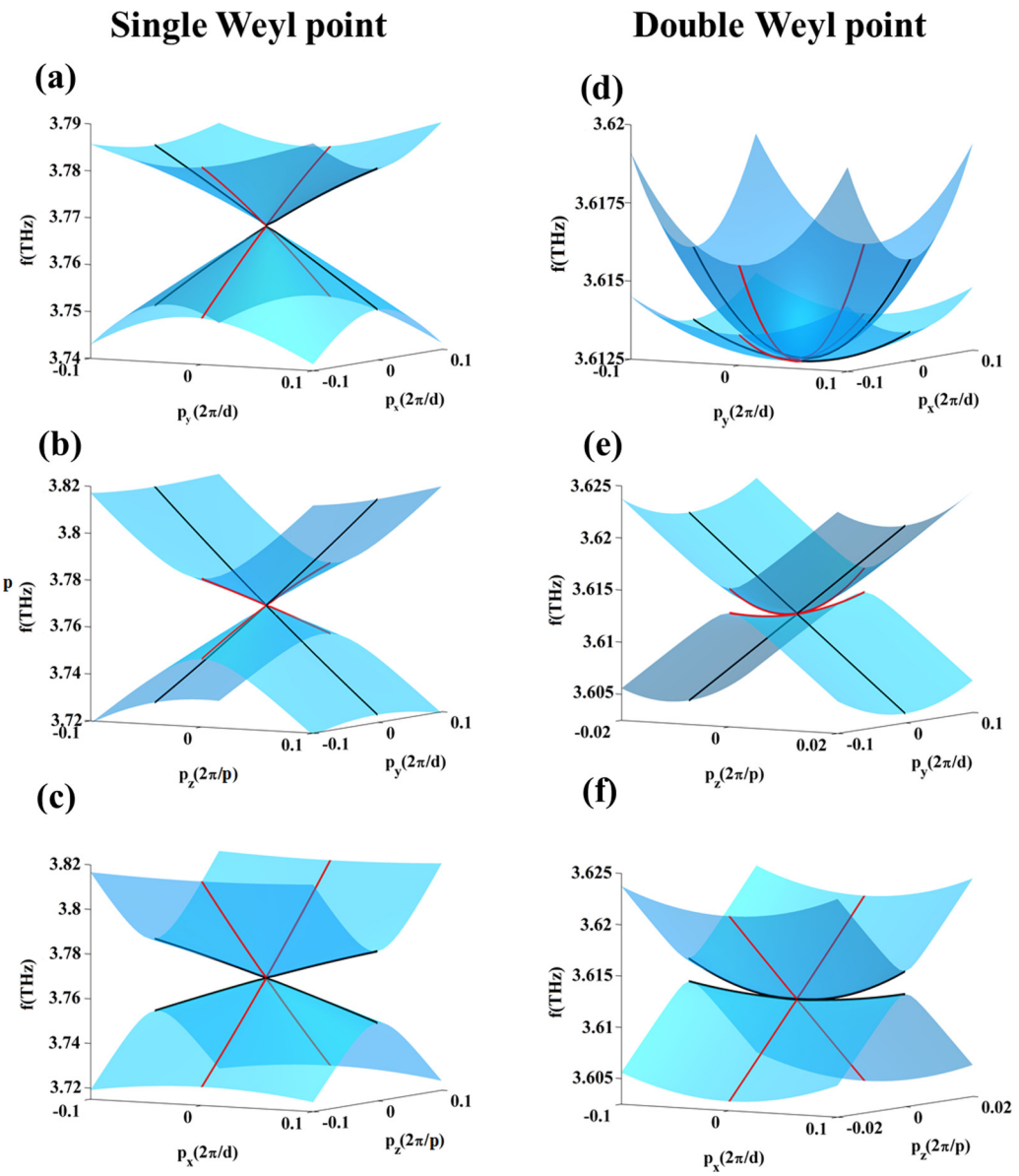

FIG. 2. Three-dimensional band structures of woodpile air-in-metal PCs around K and Γ in the directions of p_x, p_y, and p_z, respectively, calculated with COMSOL. Around K, two cones touch at K forming a nodal point, and the bands are linear along p_x, p_y, and p_z shown by the red and black lines. Around Γ, two band sheets also touch at Γ forming a nodal point. The bands are quadratic along p_x and p_y but linear along p_z. Such a Weyl point has a topological charge of 2.

at $f = 3.77\,\mathrm{THz}$ forming a nodal point in 3D momentum space around the K point. The red and black lines along the p_x, p_y, and p_z directions exhibit linear dispersions. The group velocities along p_x and p_y are the same, which is different from the group velocity along p_z. The linear dispersion indicates that the nodal point at K is a single Weyl point, consistent with our TBM result in Eq. (11a). Figures 2(d) and 2(e) also show two band sheets degenerate at $f = 3.615\,\mathrm{THz}$ forming a nodal point around Γ, but now the red and black lines are quadratic along p_x and p_y and linear along p_z. This nodal point carrying topological charge 2 is a double Weyl point, consistent with Eq. (11c). Figures 3(a)–3(c) show the band structures in the reduced Brillouin zone at $k_z = 0$, $k_z = 0.5\,\pi/p$, and $k_z = \pi/p$. The lower two bands form a single Weyl point at K and a double Weyl point at Γ at $k_z = 0$, whereas Weyl points of opposite topological charges are formed by the upper two bands at H and A at $k_z = \pi/p$. When $k_z = 0.5\,\pi/p$, these three bands separate forming two gaps as shown in Fig. 3(b). The phase of the screw rotational eigenvalues for the TBM along $K-H$ and $\Gamma-A$ are shown by the color code in Figs. 3(e) and 3(f). We can find that the phase changes continuously with k_z. Along the k_z axis, it evolves from $-\pi$ to π through these three bands. Different representations of the screw rotation eigenvalues protect the linear dispersion at these high-symmetry k points [30]. For bands with fixed k_z and if $k_z \neq 0$ and $k_z \neq \pi/p$, they are nondegenerate. These nondegenerate bands have well-defined Chern numbers. We also compare the results obtained with the TBM and COMSOL.

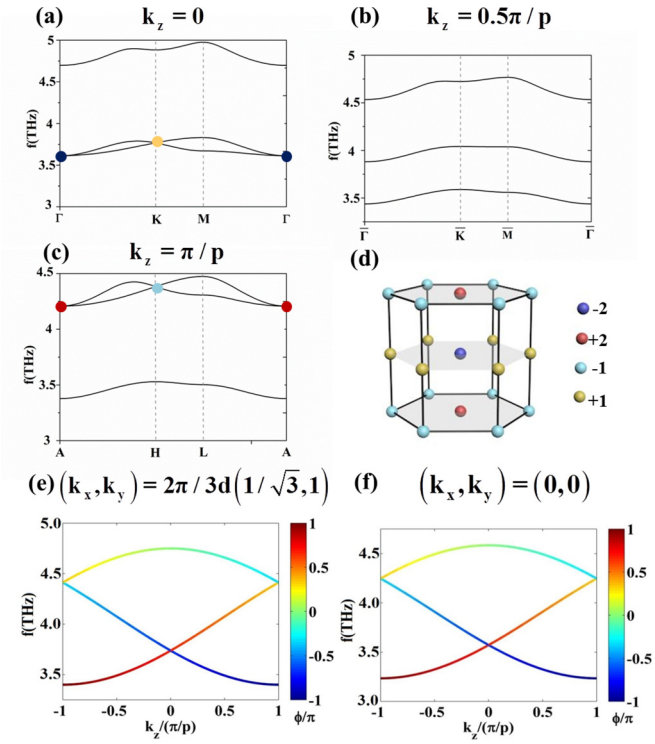

FIG. 3. The band structures of air-in-metal crystals calculated by COMSOL for (a) $k_z = 0$, (b) $k_z = 0.5\,\pi/p$, and (c) $k_z = \pi/p$. (d) The distribution of topological charges, showing ± 2 charges at Γ and A and ± 1 charges at K and H. Weyl points are found at K, H, Γ, and A. The phase of the screw rotational eigenvalues along $K-H$ and $\Gamma-A$ are shown by the color codes in (e) and (f). The bands are degenerate at these high-symmetry k points due to their different group representations, and the phase evolves from $-\pi$ to π along k_z through all three bands.

Figure 4 shows the band structure of air-in-metal woodpile PCs with the same parameters as in Fig. 2 in the whole Brillouin zone. The fitting parameters $\varepsilon = 0.804c/d$, $t_{n1} = -0.011c/d$, and $t_{n2} = 0.0675c/d$ of the TBM are obtained through fitting with the results of COMSOL. The NNN hopping is ignored because it is essentially zero in this case. The results of COMSOL and TBM qualitatively agree with each other.

The topological charges as sources or sinks of Berry flux can lead to gapless boundary modes. For the air-in-metal configuration, the effective NNN hopping t_{nnn} is essentially zero, and the sign of topological charges at the high-symmetry

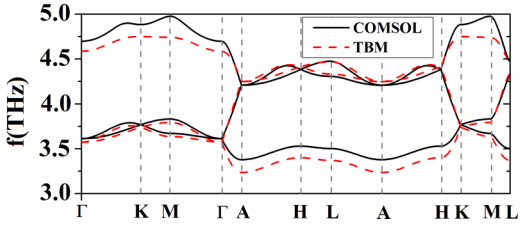

FIG. 4. The lowest three bands of the air-in-metal woodpile PCs in the whole Brillouin zone calculated by COMSOL and the TBM are shown by the black lines and red dashed lines, respectively.

points depends only on t_{n2}. The topological charge distributions obtained numerically for the real PC mentioned above are shown in Fig. 3(d). Note that the TBM [Eq. (A1)] gives the same distribution. On the $k_z = 0$ plane [Fig. 3(a)], Weyl nodes with charge $+1$ are found at K and K' (yellow dots), whereas Γ has a node with charge -2 (blue dot). On the $k_z = \pm\pi/p$ plane as shown in Fig. 3(c), Weyl nodes with charge -1 are located at H and H' (cyan dots), and A has a charge $+2$ Weyl node (red dot). The total charge on the $k_z = 0$ or $k_z = \pm\pi/p$ plane is zero, and the total Berry flux passing through any plane perpendicular to the k_z axis would vanish. The Chern number is hence zero for all the two-dimensional bands with a fixed k_z, and no topological gapless surface states can be found at truncated boundaries parallel to the z direction.

IV. SIGN CHANGE OF TOPOLOGICAL CHARGES

When the NNN hopping coefficient t_{nnn} is not negligible compared with t_{n2}, the sign of the topological charges depends not only on t_{n2}, but also on t_{nnn}. Two special cases can happen when $t_{nnn} = 0.5t_{n2}$ and $t_{nnn} = -0.25t_{n2}$. Figures 5(a)–5(c) show the band structure calculated with TBM in the Brillouin zone at $k_z = 0, \frac{0.5\,\pi}{p}, \frac{\pi}{p}$ when $t_{nnn} = 0.5t_{n2}$. We find three bands form a triply degenerate nodal line along the KH direction,

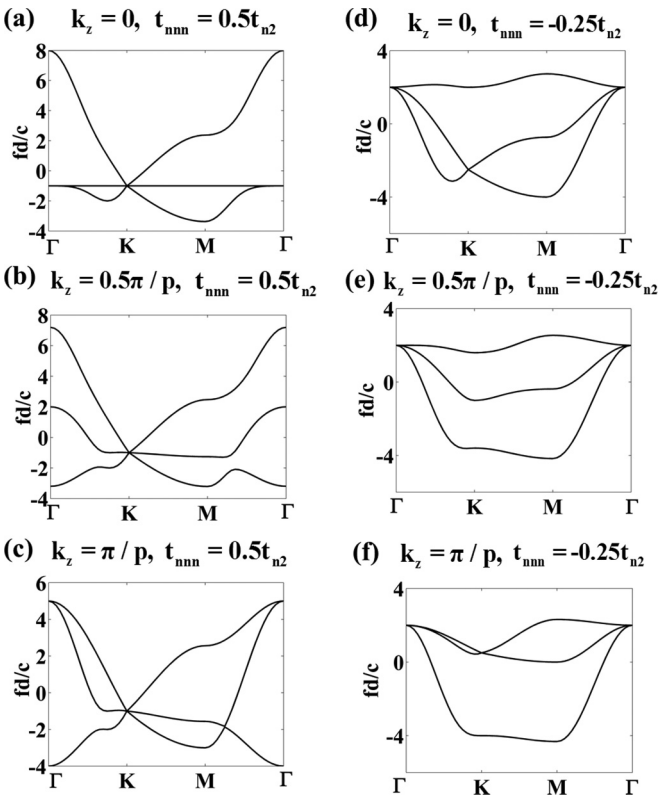

FIG. 5. The band structures at the reduced Brillouin zone at $k_z = 0$, $k_z = 0.5\,\pi/p$, and $k_z = \pi/p$ calculated with the TBM. Here we take $t_{n1} = t_{n2} = 1$. In (a)–(c), we take $t_{nnn} = 0.5t_{n2}$, three bands become accidentally degenerate along the KH direction, and the Weyl points at K and H disappear, but the double Weyl points at Γ and A still exist. When $t_{nnn} = -0.25t_{n2}$ as shown in (d)–(f), three bands are accidentally degenerate along the ΓA direction, and the double Weyl points at Γ and A disappear.

and the two Weyl points at K and H disappear while the double Weyl points at Γ and A still exist. A similar effect can also happen when $t_{nnn} = -0.25t_{n2}$ where the double Weyl points at Γ and A disappear as shown in Figs. 5(d) and 5(e), whereas those Weyl points at K and H still exist.

When the magnitude of t_{nnn} is further increased, some Weyl nodes change sign with the consequence that the total Berry flux going through any band with fixed k_z no longer vanishes. Equations (14a) and (14b) confirm that, when the NNN hopping is comparable to the interlayer hopping, topological charges at K or Γ can change sign. We will now show that this transition can happen by changing the configuration from air-in-metal to metal-in-air while keeping the geometry the same, Referring to Fig. 1(a), the NNN hopping is essentially zero if the blue rods are air and the background is metal, but for the inverse structure in which the blues rods are metal and the background is air, waves can travel in the background, which indicates that the NNN hopping cannot be zero. But of course the TBM can only suggest that the charge of the Weyl nodes could potentially switch sign. Whether the sign can actually change needs to be verified by a full wave numerical calculation for the real system, which is shown in Fig. 6. The band structures at $k_z = 0, \frac{0.5\pi}{p}, \frac{\pi}{p}$ are shown in Figs. 6(a)–6(c) for the metal-in-air configuration with the metal rods having a width and height of $b = h = 7.2\,\mu$m and the lattice constant $d = 60\mu$m. A single Weyl point exists at 3.5 THz [yellow dot in Fig. 6(a)] formed by the intersection of red and blue bands at K, whereas a node of the opposite charge exists at H [cyan dot in Fig. 6(c)]. We find two double Weyl points with opposite topological charges at Γ [red dots in Fig. 6(a)] and A [blue dots in Fig. 6(c)] each with two bands carrying quadratic dispersions on the $k_x - k_y$ plane. When $k_z = 0.5\,\pi/p$, the degeneracies are lifted, and two gaps are formed as shown in Fig. 6(b). The topological charge distribution is shown in Fig. 6(d). Compared with Fig. 3(d) for the air-in-metal configuration, the charge -2 topological nodes have a different sign. Note that a positive (negative) topological charge acts as a source (sink) of Berry flux for the upper (lower) band and a sink (source) for the lower (upper) band. Figure 6(e) shows the source/sink distributions for the red band (the lower band), which reveals that charge -1 flux sinks are located on the $k_z = 0$ plane and charge 2 flux sources are located on the $k_z = \pm\pi/p$ planes, generating Berry flux between these planes. Figures 6(f) and 6(g), respectively, show the source/sink distribution for the green band (the upper band) and the blue (middle) band. There is net Berry flux passing through the $k_z =$ constant planes for the green band but none passing through the $k_z =$ constant planes for the blue band. As a consequence, the Chern numbers of the red and green bands are -1 and $+1$, whereas it is 0 for the blue (middle) band when $k_z > 0$, which in turn implies that the gaps in Fig. 6(b) are topologically nontrivial and gapless boundary modes should exist in these gaps. To investigate the gapless surface states, we cut two surfaces in a direction perpendicular to the x axis, resulting in a strip [see Fig. 7(a)] that is periodic along the y and z directions. We cap the truncated surface with a PEC, which serves as a topologically trivial gap material. For $k_z = 0.5\,\pi/p$, we find two gapless surface states in each of these two topologically nontrivial gaps as shown in Figs. 7(b)

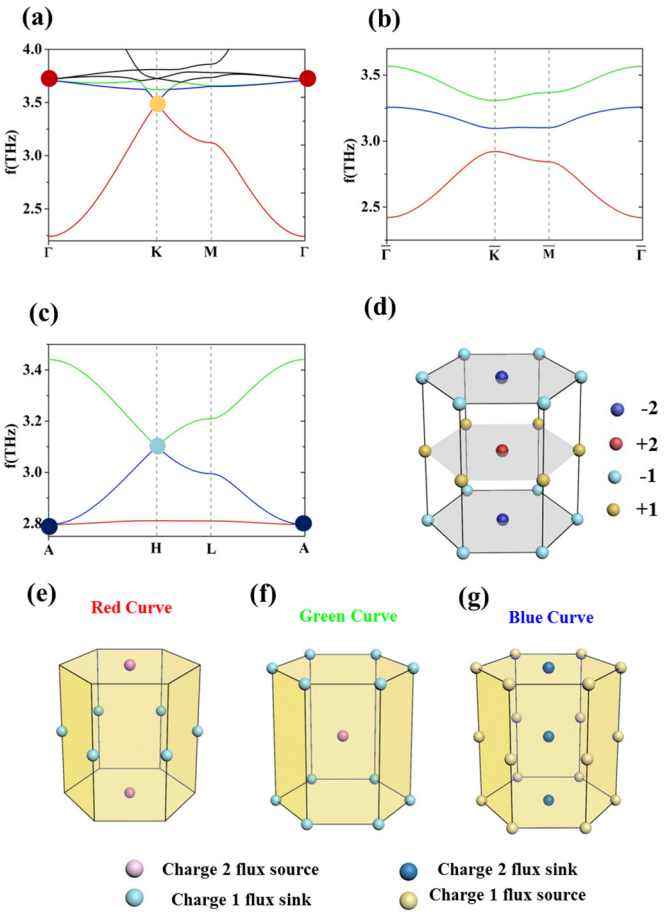

FIG. 6. The band structures of the metal-in-air configuration for (a) $k_z = 0$, (b) $k_z = 0.5\,\pi/p$, and (c) $k_z = \pi/p$. Single Weyl points are found at K and H, and double Weyl points are found at Γ and A. In (b), the calculated Chern numbers are shown. (d) Distribution of topological charges showing that the net charges on the $k_z = n\pi/p$ plane do not vanish. Weyl points as sources/sinks of Berry flux are plotted in (e)–(g) for the red, green, and blue bands.

and 7(c). The $|\mathbf{E}|$ of the two surface states shows that the fields for the blue band are located at the right boundary, propagating along $+y$ [see Figs. 7(d) and 7(f) for the lower-frequency and higher-frequency gaps, respectively], whereas the fields for the red band are located at the left boundary, propagating along $-y$ [see Figs. 7(e) and 7(g)].

The surface states should be robust against backscattering when k_z is preserved. To demonstrate this, we construct a zigzag boundary between two woodpile PCs as shown in Fig. 8. The upper PC has the air-in-metal configuration, whereas the lower PC features the metal-in-air one. The air rods and metallic rods are 33- and 12-μm wide, respectively, and both are 9-μm tall. They have the same in-plane lattice constant $d = 60\,\mu$m. According to our analysis above, these two structures should possess different topological gap properties. In the simulation, the top, left, and right boundaries are set as PECs, and the bottom boundary is set as a scattering boundary so that waves can leak out. The sample is periodic along the z direction. In Fig. 8(a), we place a line source (red star) on the left-hand side and set $k_z = -0.5\,\pi/p$. We set

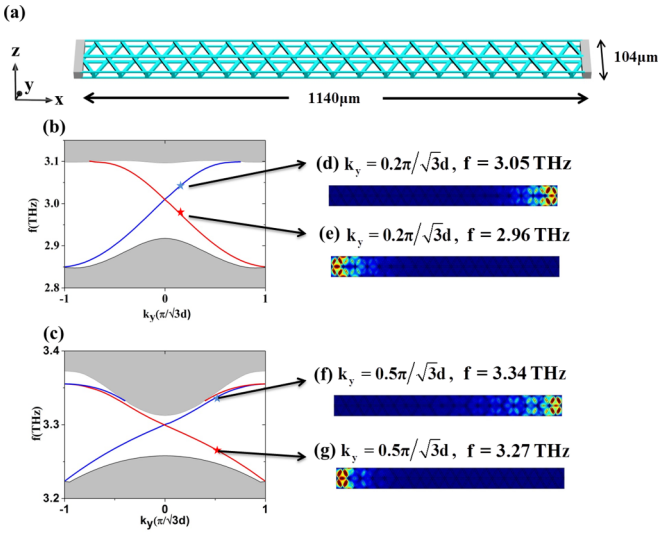

FIG. 7. (a) The slab is periodic along y and z and sandwiched between PEC slabs in the x direction. The length and width of the slabs are 1140 and 104 μm, respectively. (b) The projected band structure for $k_z = 0.5\,\pi/p$ and the parameters used here are the same as those in Fig. 3. Surface states (blue and red bands) exist in the gap near 3 THz. The bulk bands are shaded in gray. Panels (d) and (e) show the eigenfields $|\mathbf{E}|$ of the boundary modes marked by the blue and red stars, respectively, in (b) for $|k_y| = 0.2\,\pi/\sqrt{3}d$. The positive group velocity mode (blue) is located on the right surface, whereas the negative group velocity mode (red) is located on the left. Surface state properties in the higher gap near 3.3 THz are shown in panel (c). Eigenfields $|\mathbf{E}|$ of the boundary modes in panels (f) and (g) also show that the boundary modes at the right and left surfaces possess opposite group velocities along the y direction.

$f = 3.5$ THz, which is inside the common gap for both PCs. The excited surface state first propagates in the $+y$ direction on the left boundary and then turns the corner when it meets the air-in-metal PC and moves along the zigzag boundary from left to right with no backscattering. We move the source to the right as shown in Fig. 8(b) and set $k_z = 0.5\,\pi/p$. At the same frequency, waves now propagate from right to left. Note that if we use Ag instead of a PEC, the simulation results are essentially the same at $f = 3.5$ THz.

V. WEYL POINTS IN PCS WITH SILICON RODS

We emphasize that the existence of Weyl points at high-symmetry k points in the woodpile PC is a consequence of the $\tilde{C}_3$ screw symmetry and the $\tilde{C}_3$ symmetry gives us a sufficient condition to realize Weyl points (see the Appendix). The details of material and structural parameters will not affect the existence but will govern the sign of the topological charges and the details of the dispersion. For example, we also can find Weyl points in the band structure of woodpile PCs composed of silicon rods. As silicon is dielectric and possesses low loss at infrared, the sample can be fabricated, and the Weyl points can be measured at near IR or may be up to optical frequencies. Figures 9(a)–9(c) show the band structures in the reduced Brillouin zone where the width and height of the rod are $b = h = 0.132d$. We can find two single Weyl points at K and H as shown in Figs. 9(a) and 9(c). When we take $k_z = 0.48\,\pi/p$, the degeneracy at K and H will lift [see Fig. 9(e)], which shows the degenerate points are nodal points in momentum space.

Figure 10 shows the projected band structure of a strip sample where gapless surface states exist in this system at $k_z = 0.48\,\pi/p$ with fields locating at the left and right surfaces, respectively, as shown in Figs. 10(b) and 10(c). These surface states support the one-way transportation in the silicon-based woodpile structure, which makes these materials promising for controlling wave propagation on silicon-based devices. However, the band gaps in dielectric PCs are typically smaller, and so they are less robust against disorder. The band gaps in dielectric PCs can in principle be optimized by finely tuning system parameters using algorithms, such as genetic algorithms or simulated annealing. The band gaps in dielectric

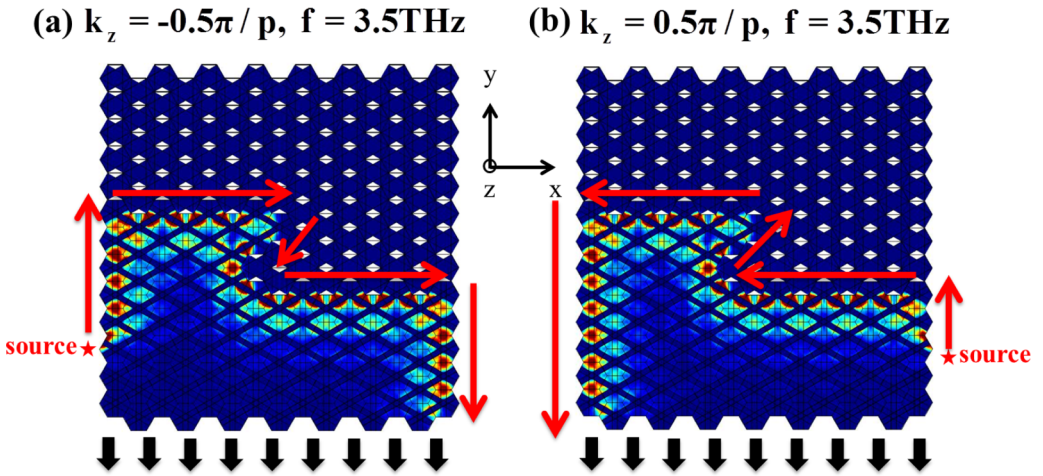

FIG. 8. One-way transport along a zigzag boundary between an upper air-in-metal and a lower metal-in-air structure. (a) When $k_z = -0.5\,\pi/p$, the edge state propagates from left to right; (b) when $k_z = 0.5\,\pi/p$, the edge state propagates from right to left. The sources are indicated by the red stars.

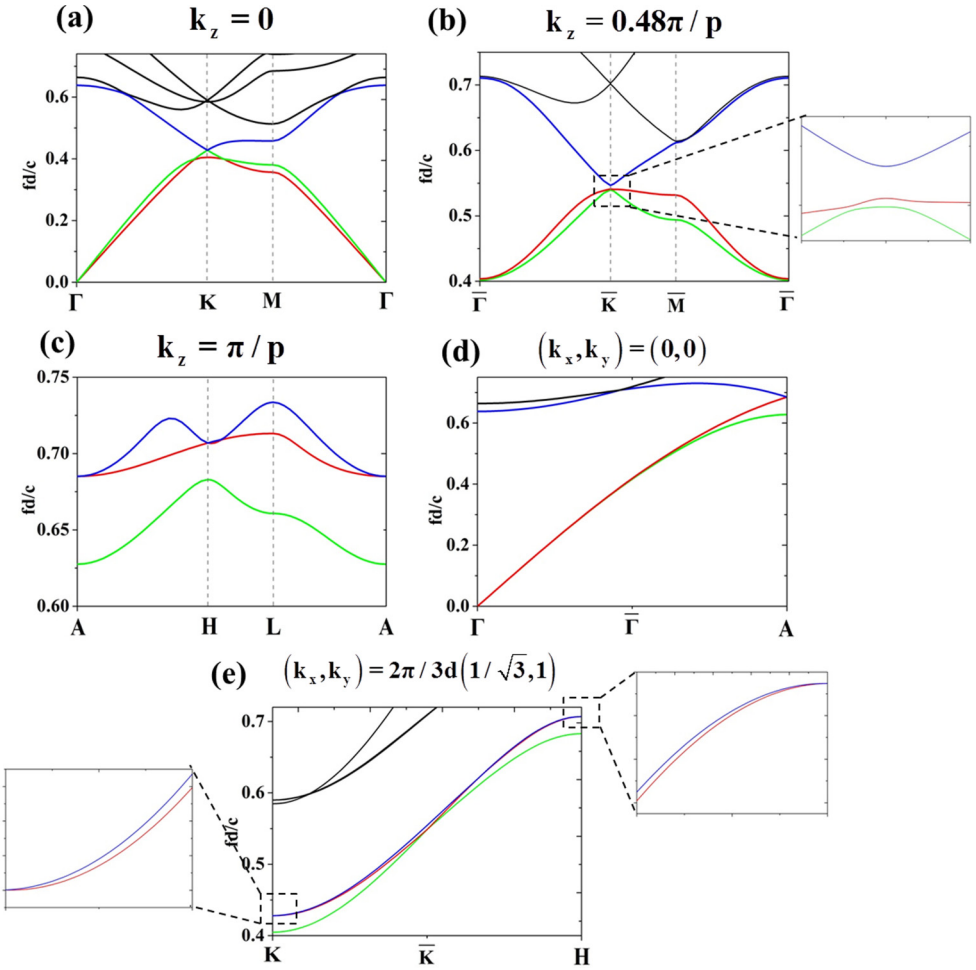

FIG. 9. Band structures of a chiral woodpile photonic crystal constructed by silicon rods in the air, where $b = h = 0.132d$ calculated using COMSOL. Green, red, and blue shows the three bands of interest. (a)–(c) Band structures in the reduced Brillouin zone with $k_z = 0$, $k_z = 0.48\,\pi/p$, and $k_z = \pi/p$, respectively. Weyl nodes with charge 1 exist in the momentum space at the K and H points with frequencies of $f = 0.43c/d$ and $f = 0.71c/d$, respectively. The inset shows the zoom in to show the bands and gaps in the vicinity of the $\bar{K}$ point. (d) and (e) Band dispersion along the ΓA and KH directions. The red and the blue bands are degenerate at $k_z = 0$ in (e). At $k_z = \pi/p$, the blue and the red bands become degenerate, and the Weyl node with charge 1 appears again. The insets of (e) indicate the band degeneracy of the red and blue bands at the ranges of $k_z \in [0, 0.1\,\pi/p]$ and $k_z \in [0.9\,\pi/p, \pi/p]$, respectively.

PCs can in principle be maximized following the similar procedures as in Ref. [30].

VI. CONCLUSION

To summarize, we have shown that metallodielectric chiral woodpile photonic crystals carry Weyl nodes with topological charges 1 and 2. Gapless surface states are found at the surface of these photonic crystal slabs. A tight-binding model shows that the sign of the topological charge can be changed by controlling the hopping range. Metallic and dielectric woodpile structures have been fabricated down to the nanoscale, making them promising platforms for achieving Weyl point-related phenomena in the high-frequency regimes. Photonic crystals are easier platforms for studying topological physics as they are not constrained by chemistry and the Fermi level, and the experiments are less demanding both in synthesis and in characterization.

ACKNOWLEDGMENTS

We thank W.-y. He for discussions. This work was supported by the Hong Kong Research Grant Council through (Grant No. AOE/P-02/12).

APPENDIX: SYMMETRY ANALYSIS

The woodpile photonic crystal system is invariant under a $\pi/6$ rotation and a simultaneous partial translation of $p/3$ along the z direction. The screw rotation operator can be written as $\tilde{C}_{6,2} \equiv \hat{C}_6 \hat{T}_{p/3}$ and hence $\tilde{C}^6_{6,2} = (\hat{T}_{p/3})^6 = \hat{T}_{2p}$ [31]. By applying the $\tilde{C}^6_{6,2}$ operator on the Bloch wave-function $\phi(\mathbf{r}) = u(\mathbf{r})e^{-i\mathbf{k}\cdot\mathbf{r}}$, we can obtain

$$\tilde{C}^6_{6,2}\phi(\mathbf{r}) = \hat{T}_{2p}\phi(\mathbf{r}) = \phi(\mathbf{r})e^{-i2k_z p}, \tag{A1}$$

which implies that the eigenvalue for the operator $\tilde{C}^6_{6,2}$ is $e^{-i2k_z p}$. Therefore the eigenvalue of the operator $\tilde{C}_{6,2}$ is $\tilde{J}_m =$

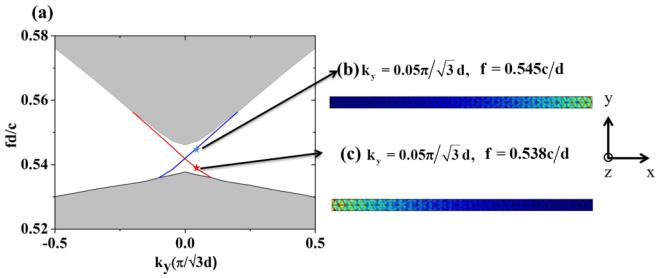

FIG. 10. (a) Bulk band structure with a silicon sample constructed with 79 unit cells around the frequency of the nontrivial photonic band gap, calculated using COMSOL. The left and right surfaces of the sample are terminated with PEC boundaries, which serve as a gap material for the photon. The sample is periodic along the y and z directions with $k_z = 0.48\,\pi/p$. Two edge states with opposite group velocity exist inside the gap. (b) and (c) Eigenfield $|\mathbf{E}|$ patterns show that, at $k_y = 0.05\,\pi/\sqrt{3}d$, the blue bands with positive group velocity are located at the left surface whereas the fields of the red band with negative group velocity are located at the right surface.

$J_m e^{-ik_z p\beta}$ with $J_m = e^{im\pi\beta}$ being the rotation eigenvalue and $m \in \{0\text{–}5\}$. At the k_z zone boundaries where $k_z = \pm\pi/p$, we have

$$\begin{aligned}\tilde{J}_0(k_z p/3) &= \tilde{J}_2(k_z p/3 + 2\pi/3),\\ \tilde{J}_2(k_z p/3) &= \tilde{J}_4(k_z p/3 + 2\pi/3),\\ \tilde{J}_4(k_z p/3) &= \tilde{J}_0(k_z p/3 + 2\pi/3),\end{aligned} \tag{A2a}$$

$$\begin{aligned}\tilde{J}_1(k_z p/3) &= \tilde{J}_3(k_z p/3 + 2\pi/3),\\ \tilde{J}_3(k_z p/3) &= \tilde{J}_5(k_z p/3 + 2\pi/3),\\ \tilde{J}_5(k_z p/3) &= \tilde{J}_1(k_z p/3 + 2\pi/3),\end{aligned} \tag{A2b}$$

since the eigenvalues for different representations of screw symmetry connect states with $\Delta m = 2$ at the k_z boundaries. Hence as shown in Eq. (A2), bands with screw rotational eigenvalues $\tilde{J}_0$, $\tilde{J}_2$, and $\tilde{J}_4$ (or $\tilde{J}_1$, $\tilde{J}_3$, and $\tilde{J}_5$) should connect at the zone boundaries in the extended Brillouin zone, processing a periodicity of $k_z = 6\,\pi/p$. Figure 11(a) shows the general dispersions of three bands along the ΓA direction in the extended zone scheme. When the bands in the extended zone fold back to the first Brillouin zone [Fig. 11(b)], two unavoidable crossings inside the first Brillouin zone will occur as shown in Fig. 11(b). Meanwhile, if the system possesses the time-reversal symmetry, then

$$T H(0,0,k_z) T^{-1} = H(0,0,-k_z). \tag{A3}$$

Equation (A4) indicates that the bands (in an extended zone scheme) must be symmetric with respecte to $k_z = 0$ along the ΓA direction as shown in Fig. 11(c) for systems possessing time-reversal symmetry. Hence when these bands cross each other, these crossing points must be at $k_z = 0$ or $k_z = \pm\pi/p$. A typical band structure is shown in Fig. 11(d) with the bands folded back to the first Brillouin zone where we have two linear crossing points, one at the Γ point and another at the A point.

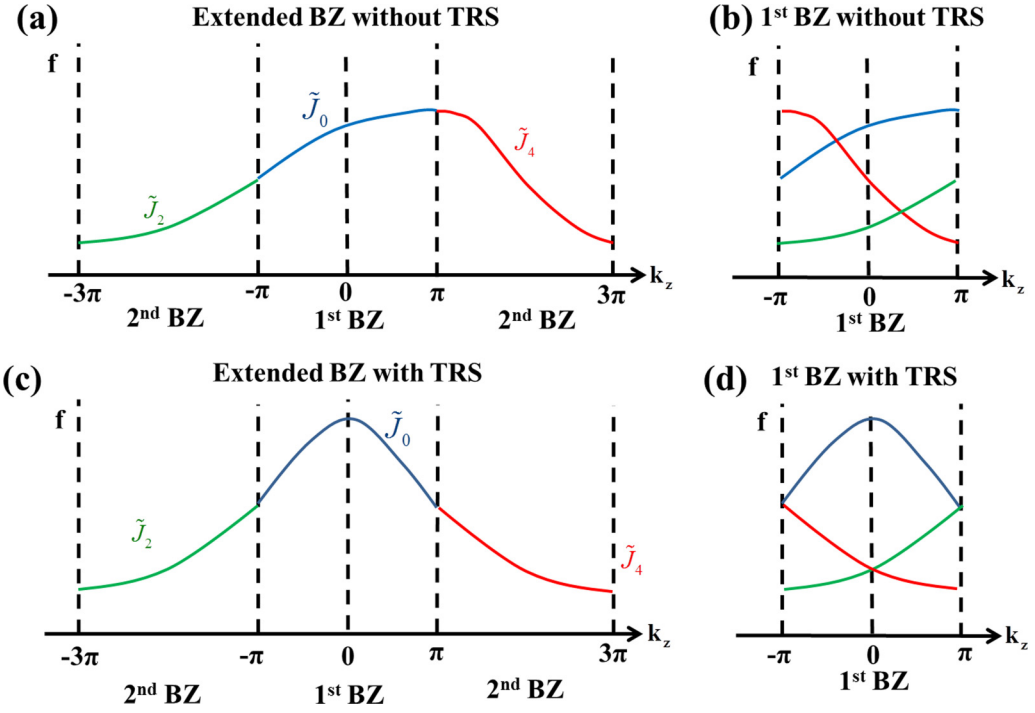

FIG. 11. Bands with different eigenvalues of screw symmetry along the ΓA axis connect smoothly at the k_z boundaries. (a) When time-reversal symmetry is broken and only the $\tilde{C}_3$ symmetry is in the system, the bands with $\tilde{J}_0$, $\tilde{J}_2$, and $\tilde{J}_4$ connect at the k_z boundaries. (b) These bands form unavoidable crossings when they fold back to the first Brillouin zone, and the crossing points can be located at arbitrary k_z. (c) When time-reversal symmetry is present as $E_{\tilde{J}_2}(k_z) = E_{\tilde{J}_4}(-k_z)$ and $E_{\tilde{J}_0}(k_z) = E_{\tilde{J}_0}(-k_z)$, which indicates the bands with $\tilde{J}_2$ and $\tilde{J}_4$ should be symmetric and the $\tilde{J}_0$ band should be symmetric about $k_z = 0$. (d) After band folding, the crossing bands should locate at $k_z = 0$ and $k_z = \pm\pi/p$. Similarly, the bands crossing along KH can be analyzed by the same method.

At Γ where two bands cross, we can apply the $\tilde{C}_{6,2}$ operator on the Hamiltonian and have

$$\tilde{C}_{6,2}H(\mathbf{k})\tilde{C}_{6,2}^{-1} = H(R_6\mathbf{k}). \tag{A4}$$

where R_6 is the sixfold rotational operation. Then if we choose the eigenfunctions of $\tilde{C}_{6,2}$ as the basis, at the Γ point, the matrix representation of $\tilde{C}_{6,2}$ can be presented as

$$\tilde{C}_{6,2} = e^{i[(m_1+m_2)/6]\pi}e^{i[(m_1-m_2)/6]\pi\sigma_z}e^{-ik_zp/3}, \tag{A5}$$

where m_1 and m_2 are the eigenvalues of $\tilde{C}_{6,2}$ of two crossing bands. Near this two-band degenerate point, the general form of effective Hamiltonian can be written as

$$H(\mathbf{k}) = d(\delta\mathbf{k})\sigma_+ + d^*(\delta\mathbf{k})\sigma_- + g(\delta\mathbf{k})\sigma_z, \tag{A6}$$

where $\sigma_\pm = \sigma_x \pm i\sigma_y$, $\delta\mathbf{k}$ represents the wave vector deviating from Γ on the xy plane, and $g(\delta\mathbf{k})$ and $d(\delta\mathbf{k})$ are general real and complex functions, respectively. We assume that the eigenvalues of these two degenerate bands are $\tilde{J}_{m_1}(k_z = 0)$ and $\tilde{J}_{m_2}(k_z = 0)$, respectively. From the discussion above, we have $|m_1 - m_2| = 2$. By applying the operator $\tilde{C}_{6,2}$ on the effective Hamiltonian (A6), we can obtain

$$\begin{aligned}\tilde{C}_{6,2}H(\mathbf{k})\tilde{C}_{6,2}^{-1} = {} & d(\delta\mathbf{k})e^{i[(m_1-m_2)3]\pi}\sigma_+ \\ & + d^*(\delta\mathbf{k})e^{-i[(m_1-m_2)/3]\pi}\sigma_- + g(\delta\mathbf{k})\sigma_z.\end{aligned} \tag{A7}$$

Meanwhile, $R_6\mathbf{k}$ is given by

$$R_6(k_+,k_-) = (k_+e^{i\pi/3},k_-e^{i\pi/3}), \tag{A8}$$

where $k_\pm = k_x \pm ik_y$. By substituting Eqs. (A7) and (A8) into Eq. (A5), we have

$$e^{-i[(m_1-m)/3]\pi}d(\delta k_+,\delta k_-) = d(\delta k_+e^{i\pi/3},\delta k_-e^{i\pi/3}), \tag{A9a}$$

$$g(\delta k_+,\delta k_-) = g(\delta k_+e^{i\pi/3},\delta k_-e^{i\pi/3}). \tag{A9b}$$

Expanding $d(\delta\mathbf{k})$ and $g(\delta\mathbf{k})$ with respect to (k_+,k_-) gives

$$d(\delta k_+,\delta k_-) = \sum_{n_1,n_2} A_{n_1n_2}\delta k_+^{n_1}\delta k_-^{n_2}, \tag{A10a}$$

$$g(\delta k_+,\delta k_-) = \sum_{n_1,n_2} B_{n_1n_2}\delta k_+^{n_1}\delta k_-^{n_2}, \tag{A10b}$$

where $A_{n_1n_2}$ and $B_{n_1n_2}$ are complex coefficients. By substituting Eq. (A10) into Eq. (A9), we find the norvanishing terms are A_{02}, A_{20}, and B_{00} if we retain the lowest order. The effective Hamiltonian can then be written as

$$H(\delta\mathbf{k}) = v_z\delta k_z\sigma_z + A_{20}\delta k_+^2\sigma_+ + A_{02}\delta k_-^2\sigma_+ + \text{H.c.} \tag{A11}$$

From Eqs. (A2) and (A11), we see double Weyl points are formed at the high-symmetry k point along k_z at Γ and A. Also we can study the effective Hamiltonian around the K (H) point. As the point-group symmetry of the k_z axis at K is only $\tilde{C}_{3,1}$, the eigenvalues of $\tilde{C}_{3,1}$ is $\tilde{J}_m = J_me^{-ik_zp/3}$ where $J_m = e^{i(2m\pi/3)}$ and $m \in \{0,1,2\}$. At the k_z boundary, the eigenvalues have the relation,

$$\begin{aligned}\tilde{J}_0(k_zh) &= \tilde{J}_1(k_zh+2\pi/3),\\ \tilde{J}_1(k_zh) &= \tilde{J}_2(k_zh+2\pi/3),\\ \tilde{J}_2(k_zh) &= \tilde{J}_0(k_zh+2\pi/3).\end{aligned} \tag{A12}$$

As the difference in the eigenvalues of two degenerate bands is $\Delta m = m_1 - m_2 = 1$, the constraint as Eqs. (A9a) and (A9b) can be written as

$$e^{-i[2(m_1-m_2)/3]\pi}d(\delta k_+,\delta k_-) = d(\delta k_+e^{i2\pi/3},\delta k_-e^{i2\pi/3}), \tag{A13a}$$

$$g(\delta k_+,\delta k_-) = g(\delta k_+e^{i2\pi/3},\delta k_-e^{i2\pi/3}). \tag{A13b}$$

Therefore only terms of A_{01} and A_{10} survive for d, and terms of B_{00} survive for g. The effective Hamiltonian has the form of

$$H(\delta\mathbf{k}) = v_z\delta k_z\sigma_z + A_{10}\delta k_+\sigma_+ + A_{01}\delta k_-\sigma_+ + \text{H.c.}, \tag{A14}$$

which indicates a Weyl node with charge 1 at K or H.

[1] S.-M. Huang *et al.*, Nat. Commun. **6**, 7373 (2015).
[2] B. Q. Lv *et al.*, Nat. Phys. **11**, 724 (2015).
[3] A. A. Soluyanov, D. Gresch, Z. Wang, Q. Wu, M. Troyer, X. Dai, and B. A. Bernevig, Nature (London) **527**, 495 (2015).
[4] S.-Y. Xu *et al.*, Nat. Phys. **11**, 748 (2015).
[5] L. X. Yang, Z. K. Liu, Y. Sun, H. Peng, H. F. Yang, T. Zhang, B. Zhou, Y. Zhang, Y. F. Guo, M. Rahn, D. Prabhakaran, Z. Hussain, S.-K. Mo, C. Felser, B. Yan, and Y. L. Chen, Nat. Phys. **11**, 728 (2015).
[6] T. Dubček, C. J. Kennedy, L. Lu, W. Ketterle, M. Soljačić, and H. Buljan, Phys. Rev. Lett. **114**, 225301 (2015).
[7] A. A. Burkov, M. D. Hook, and L. Balents, Phys. Rev. B **84**, 235126 (2011).
[8] L. Lu, L. Fu, J. D. Joannopoulos, and M. Soljačić, Nat. Photonics **7**, 294 (2013).
[9] L. Lu, Z. Wang, D. Ye, L. Ran, L. Fu, J. D. Joannopoulos, and M. Soljačić, Science **349**, 622 (2015).
[10] M. Xiao, W.-J. Chen, W.-Y. He, and C. T. Chan, Nat. Phys. **11**, 920 (2015).
[11] W.-J. Chen, M. Xiao, and C. T. Chan, Nat. Commun. **7**, 13038 (2016).
[12] M. Xiao, Q. Lin, and S. Fan, Phys. Rev. Lett. **117**, 057401 (2016).
[13] J. Bravo-Abad, L. Lu, L. Fu, H. Buljan, and M. Soljačić, 2D Mater. **2**, 034013 (2015).
[14] W. Gao, B. Yang, M. Lawrence, F. Fang, B. Béri, and S. Zhang, Nat. Commun. **7**, 12435 (2016).
[15] L. Wang, S.-K. Jian, and H. Yao, Phys. Rev. A **93**, 061801(R) (2016).
[16] H. Weyl, Z. Phys. **56**, 330 (1929).

[17] K. M. Ho, C. T. Chan, C. M. Soukoulis, R. Biswas, and M. Sigalas, Solid State Commun. **89**, 413 (1994).
[18] S. Noda, K. Tomoda, N. Yamamoto, and A. Chutinan, Science **289**, 604 (2000).
[19] S. Takahashi, K. Suzuki, M. Okano, M. Imada, T. Nakamori, Y. Ota, K. Ishizaki, and S. Noda, Nature Mater. **8**, 721 (2009).
[20] J. G. Fleming, S. Y. Lin, I. El-Kady, R. Biswas, and K. M. Ho, Nature (London) **417**, 52 (2002).
[21] K. H. Fung, J. C. W. Lee, and C. T. Chan, arXiv:0811.1438.
[22] G. Shvets and I. Tsukerman, *Plasmonics and Plasmonic Metamaterials: Analysis and Applications* (World Scientific, Singapore, 2012).
[23] S. Takahashi, T. Tajiri, Y. Ota, J. Tatebayashi, S. Iwamoto, and Y. Arakawa, Appl. Phys. Lett. **105**, 051107 (2014).
[24] S. Endo, T. Oka, and H. Aoki, Phys. Rev. B **81**, 113104 (2010).
[25] J. Mei, Y. Wu, C. T. Chan, and Z.-Q. Zhang, Phys. Rev. B **86**, 035141 (2012).
[26] K. Sun, W. V. Liu, A. Hemmerich, and S. Das Sarma, Nat. Phys. **8**, 67 (2012).
[27] C. Fang, M. J. Gilbert, X. Dai, and B. A. Bernevig, Phys. Rev. Lett. **108**, 266802 (2012).
[28] D. Xiao, M.-C. Chang, and Q. Niu, Rev. Mod. Phys. **82**, 1959 (2010).
[29] S. Oono, T. Kariyado, and Y. Hatsugai, Phys. Rev. B **94**, 125125 (2016).
[30] S. G. Johnson and J. D. Joannopoulos, Appl. Phys. Lett. **77**, 3490 (2000).
[31] B.-J. Yang, T. Morimoto, and A. Furusaki, Phys. Rev. B **92**, 165120 (2015).